MDPI

Urban Land Surface Temperature Downscaling in Chicago: Addressing Ethnic Inequality and Gentrification

Jangho Lee [1,*], Max Berkelhammer [1], Matthew D. Wilson [2], Natalie Love [3] and Ralph Cintron [4]

1 Department of Earth and Environmental Sciences, University of Illinois Chicago, Chicago, IL 60607, USA; berkelha@uic.edu
2 Great Cities Institute, University of Illinois Chicago, Chicago, IL 60607, USA; mwilso25@uic.edu
3 Department of Biological Sciences, University of Illinois Chicago, Chicago, IL 60607, USA; nlove@uic.edu
4 Department of Latin American and Latino Studies, University of Illinois Chicago, Chicago, IL 60607, USA; rcintron@uic.edu
* Correspondence: jholee@uic.edu

Abstract: In this study, we developed a XGBoost-based algorithm to downscale 2 km-resolution land surface temperature (LST) data from the GOES satellite to a finer 70 m resolution, using ancillary variables including NDVI, NDBI, and DEM. This method demonstrated a superior performance over the conventional TsHARP technique, achieving a reduced RMSE of 1.90 °C, compared to 2.51 °C with TsHARP. Our approach utilizes the geostationary GOES satellite data alongside high-resolution ECOSTRESS data, enabling hourly LST downscaling to 70 m—a significant advancement over previous methodologies that typically measure LST only once daily. Applying these high-resolution LST data, we examined the hottest days in Chicago and their correlation with ethnic inequality. Our analysis indicated that Hispanic/Latino communities endure the highest LSTs, with a maximum LST that is 1.5 °C higher in blocks predominantly inhabited by Hispanic/Latino residents compared to those predominantly occupied by White residents. This study highlights the intersection of urban development, ethnic inequality, and environmental inequities, emphasizing the need for targeted urban planning to mitigate these disparities. The enhanced spatial and temporal resolution of our LST data provides deeper insights into diurnal temperature variations, crucial for understanding and addressing the urban heat distribution and its impact on vulnerable communities.

1. Introduction

Remotely sensed estimates of land surface temperature (LST) in urban areas are a critical metric for evaluating urban climate conditions, particularly in examining the surface urban heat island effect and understanding the influence of urban climate on societal and environmental aspects [1–4]. The high-resolution mapping of LST in urban areas has emerged as a vital tool for assessing environmental justice [5,6] and varying heat exposures at the neighborhood scale [7,8], as LST is highly sensitive to urban elements such as land covers [9,10] and vegetation [11–13]. However, a detailed estimation of LST with a neighborhood-scale spatial resolution and temporal resolution to capture diurnal cycles and extreme events are lacking, underscoring a gap in how high LST in cities varies with socioeconomic factors.

Polar-orbiting satellites such as MODIS [14–17] or the Landsat series [2,12,18] are extensively used for detailed urban LST estimates due to their high spatial resolution (up to 60 m). However, their primary limitation is that they are designed with a fixed return time—that they revisit the same region on Earth at fixed hour of the day—restricting continuous LST monitoring or diurnal cycle analysis. ECOSTRESS, mounted on the International Space Station (ISS), has the potential to address this by revisiting locations irregularly, offering

insights into the diurnal characteristics of LST while maintaining the high spatial resolution of 70 m. Although it cannot provide continuous estimates and has long return periods, it has been widely utilized for LST analysis [19–23]. For example, it has been utilized for analyzing the diurnal dynamics of surface urban heat island [24], impact of urban landscapes on LST [25], and various factors affecting LST [26].

On the other hand, geostationary satellites, especially the GOES-R series, stand out for their ability to continuously monitor a fixed point on Earth, making them ideal for the sub-hourly LST data capture over North America, despite their lower spatial resolution (2 km) compared to polar-orbiting satellites. This capability has led to their increasing use in urban LST monitoring [27–30].

To maximize the benefits of these varied satellite systems, previous studies have presented methods to improve the spatial resolution of LST estimates through downscaling. This process often involves using statistical method with ancillary parameters, such as the Normalized Difference Vegetation Index (NDVI) [19,31,32], available at finer resolutions. One prominent example using NDVI for downscaling is the TsHARP approach [32] which utilize NDVI to establish a linear relationship with LST for downscaling. However, in diverse urban environments, these NDVI-based methods can be subject to large errors due to the influence of other factors like elevation and urban structures [33–35]. Thus, other ancillary parameters such as the Normalized Difference Built-up Index (NDBI), and Digital Elevation Models (DEM) [36,37] are often used to address this limitation.

Additionally, more sophisticated statistical methods incorporating multiple predictor variables and non-linear relationships have been explored. These include machine-learning and deep-learning techniques such as Random Forest [12,38], Artificial Neural Networks [39,40], and Extreme Gradient Boosting (XGBoost) [41]. These methods are particularly effective in complex spatial data analysis due to their ability to capture non-linear interactions and handle multicollinearity among predictors. However, they also present challenges, including the potential for overfitting and increased computation demands. Thus, the detailed pre-processing and robust tuning of the data and models are essential during the development phase.

One of the primary motivations to generate downscaled LST products is to develop a better understanding of how exposure to heat—the primary cause of weather-related mortality [42]—varies with factors such as ethnicity and economic status. Demographic gradients in cities are steep—often varying significantly block to block—and, thus, data at this resolution are needed. The unequal exposure to LST among different socioeconomic groups has recently been the focus of multiple studies [5,6,43–45]. Especially, environmental inequality from an ethnic perspective has been a concern, especially in large cities in the US [46,47]. It is critical to document the exposure of minoritized and/or marginalized groups to higher temperatures because these groups often lack the resources and domestic infrastructure to mitigate the impact of heat. This disparity makes existing socioeconomic inequalities more significant and poses risks to public health, particularly during heat waves and extreme weather events. Additionally, the vulnerability of these communities to the urban heat island effect is further intensified by their limited access to cooling facilities and green spaces, a situation exemplified in documented cases from Chicago [48,49].

In this study, our first objective is to develop an XGBoost-based downscaling method for LST and compare its performance with the conventional TsHARP model, specifically focusing on the Chicago region in the summertime of 2019–2023. Secondly, our study extends the outcome of the downscaling to illustrate practical applications of an hourly 70 m LST for a major urban center. We demonstrate how these downscaled LST datasets can be effectively utilized to classify ethnic inequalities associated with exposure to high LST.

2. Data

2.1. LST Data

In this study, LST data come from two primary sources. The first is the LST estimates from GOES-16, 17, and 18 satellites, hereafter collectively referred to as GOES [50]. These

estimates, which serve as the basis for our downscaling, have a spatial resolution of 2 km and provide hourly estimates. For our analysis, we extract data specific to the urban, suburban, and preurban regions around Chicago during the summer months (June, July, and August) spanning 5 years from 2019 to 2023. The specific study region and its local climate zones [51] are depicted in Figure 1. Previous studies have reported error margin of GOES LST to be below 2 K [52,53].
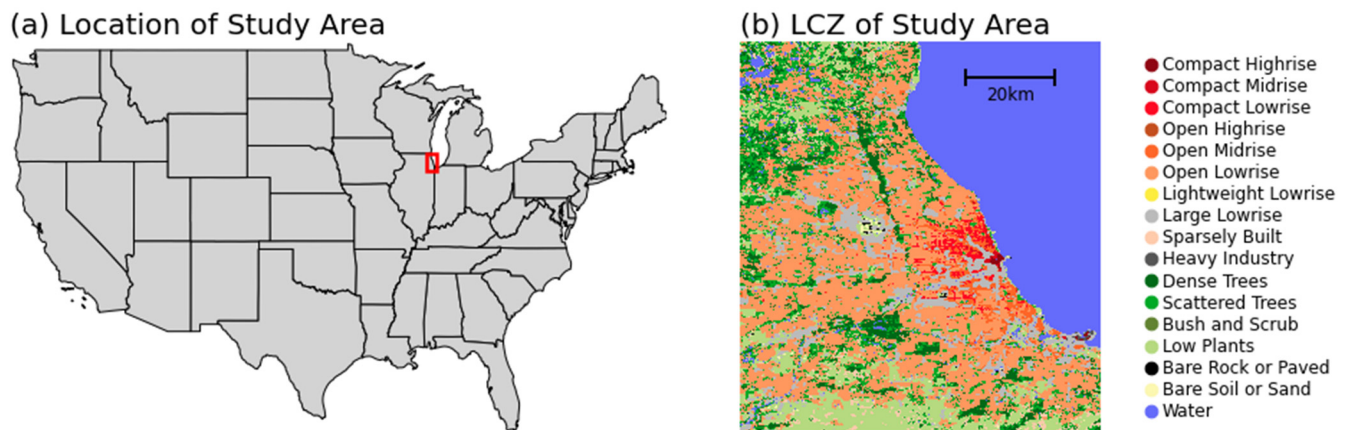

Figure 1. Location and land use characteristics of the study area. (**a**) A red box on the map of the US highlights the study region. (**b**) Local climate zones within the study area, providing an overview of different land use patterns.

The second source of LST data in our study is from ECOSTRESS LST estimates onboard the International Space Station (ISS). ECOSTRESS has a finer spatial resolution of 70 m but has an irregular revisit period for the Chicago area. Additionally, due to the unique orbit of the ISS, not all parts of Chicago are observed in each pass. Therefore, we have utilized ECOSTRESS data whenever it captures part or all our study region within its scene. Over the five-year span of our study period, this approach yielded a total of 221 scenes. Previous studies have reported a mean absolute error of the ECOSTRESS LST product to be below 0.5 K [54].

One inherent limitation of satellite-based LST estimates is the inability to measure LST under a cloud cover. To address this issue, we have utilized a cloud mask and quality control products from both GOES and ECOSTRESS, using only a 'best-quality' LST product—with a minimal cloud edge and shadow effect. By applying these cloud masks, we effectively filter out any LST data obscured by clouds. Consequently, the LST data we use for both GOES and ECOSTRESS in our study can be considered as cloud-free LST estimates. The average LST for ECOSTRESS and GOES for the entire study period can be found in Figure 2a,b.

2.2. Ancillary Variables

In this study, we utilize three ancillary variables: the Normalized Difference Vegetation Index (NDVI), the Normalized Difference Built-up Index (NDBI), and the digital elevation map (DEM). These variables are selected since they are closely related to the LST variation, especially in urban settings [10,55–57]. The NDVI and NDBI datasets are sourced from Sentinel-2 imagery [58], which provides a high spatial resolution of 10 m and a revisit period of 10 days. The calculation of NDVI and NDBI are performed as Equations (1) and (2):

$$\text{NDVI} = \frac{\text{NIR} - \text{RED}}{\text{NIR} + \text{RED}} \tag{1}$$

$$\text{NDBI} = \frac{\text{SWIR} - \text{NIR}}{\text{SWIR} + \text{NIR}} \tag{2}$$

In Equations (1) and (2), NIR, RED, and SWIR corresponds to the near-infrared (central wavelength: 0.842 μm), red (0.665 μm), and short-wave infrared (1.610 μm) bands of Sentinel-2, respectively. NDVI exhibits a clear seasonal cycle as it is related to the vegetation, whereas NDBI shows minimal variation during the summer months. Given this, for NDVI values, we use daily values. Since NDVI values are available in a 10-day frequency due to the revisit frequency of Sentinel-2, we temporally interpolate the NDVI values to a daily resolution. For the NDBI, we use annual values which are the median NDBI values for the entire summer months of that year. Over the 5-year study period, this approach results in a total of 460 NDVI data maps (92 days × 5 years) and 5 NDBI maps (5 years).

The DEM dataset comes from the 1/3 arc-second (approximately 10 m) map from the US Geological Survey [59,60]. We have chosen the 2017 DEM dataset for our study region, as it provides the most up-to-date data available for our area of interest. These 2017 DEM data are employed as a static variable map, consistently used across the entire study period from 2019 to 2023. From the DEM map, we extract the elevation (ELEV) for our analysis. Visualizations of these ancillary variables, including NDVI, NDBI, and ELEV, are presented in Figure 2c–e.
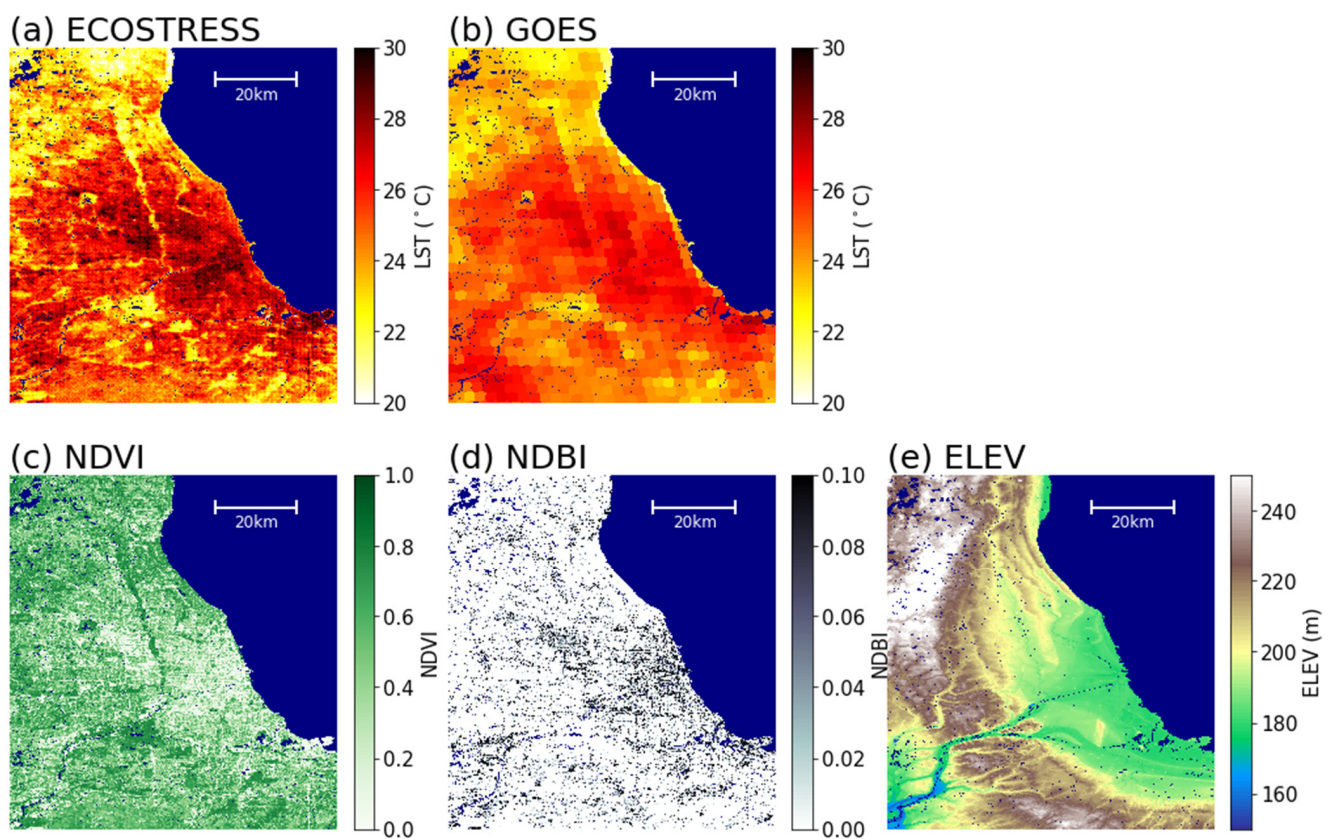

Figure 2. Data visualizations for the study, with permanent water bodies masked out in navy. (**a**) Cloud-free average LST from ECOSTRESS with 70 m resolution for the entire study period. (**b**) Same as (**a**), but for GOES estimates with 2 km resolution. (**c**) Average NDVI data with 10 m resolution for the study period. (**d**) Similar to (**c**), but for NDBI. Note that NDBI values range from 0 to 1. However, for better visualization, the color bar is scaled from 0 to 0.1, since NDBI map contains a high frequency of values near zero. (**e**) 10 m-resolution ELEV map for the year 2017, derived from DEM data.

2.3. Collocation and Aggregation of Data

Given the irregular observation frequency of ECOSTRESS and the continuous hourly measurements provided by GOES, we first align the GOES data temporally with ECOSTRESS scenes. To achieve this, we identify two GOES scenes that temporally bracket each

ECOSTRESS scene. We then calculate a weighted average of these two GOES scenes, using weights inversely proportional to their temporal distance from the corresponding ECOSTRESS scene. This process results in GOES data that are temporally aligned to the ECOSTRESS timestamps. The collocated LST estimates from GOES and ECOSTRESS will be referred to as $\text{LST}_{2\text{km}}$ and $\text{LST}_{70\text{m}}$, respectively.

As a next step, we aggregate ancillary variables to align with the GOES and ECOSTRESS data. For each GOES grid point, we define a circle with a radius of 1 km, which is half of the GOES's native resolution. Within this circle, we average the 10 m-resolution values of NDVI, NDBI, and ELEV to derive aggregated values at the 2 km resolution for each of these variables. This method ensures that the higher-resolution data are appropriately scaled to match the coarser spatial resolution of the GOES dataset. These averaged variables are then denoted as $\text{NDVI}_{2\text{km}}$, $\text{NDBI}_{2\text{km}}$, and $\text{ELEV}_{2\text{km}}$, respectively. This aggregation process ensures that the ancillary data are consistent with the spatial resolution of the LST data from GOES. The same procedure is applied to ECOSTRESS grid points with a 35 m radius to generate $\text{NDVI}_{70\text{m}}$, $\text{NDBI}_{70\text{m}}$, and $\text{ELEV}_{70\text{m}}$.

2.4. Socioeconomic Data

In addition to meteorological and land cover data, we utilize socioeconomic data in this study. The ethnic demographic data for Chicago are sourced from the 2020 Decennial Census of the U.S. Census Bureau. Organized at the block level, this dataset covers 38,783 city blocks with an average block size of 0.015 km^2 and standard deviation of area of 0.103 km^2. Each block details population counts for total, White, Black, Asian, and Hispanic/Latino groups. The ethnic composition of Chicago's population is as follows: 32.5% White, 29.61% Black, 7.14% Asian, and 30.80% Hispanic/Latino. Additionally, we utilize the economic hardship and education level (population with high school diploma) which come in at a block group level, which is a group of multiple-block-level data.

3. Downscaling Methods

3.1. TsHARP-Based Method

In our study, we employ a modified version of the TsHARP method [32], a widely used method to downscale LST [31,61–63], as a baseline model. The TsHARP method establishes a linear relationship between the NDVI and LST, using it to generate LST data at the finer resolution of the NDVI map. Mathematically, this can be expressed as Equation (3):

$$\text{LST}_{\text{fine}}(s) = \alpha(s) \times (\text{NDVI}_{\text{coarse}}(s) - \text{NDVI}_{\text{fine}}(s)) + \text{LST}_{\text{coarse}}(s) + \varepsilon(s) \tag{3}$$

In Equation (3), LST_{fine} and $\text{LST}_{\text{coarse}}$ each represents the LST at fine and coarse resolutions, respectively, corresponding to ECOSTRESS and GOES LST products in this study. $\text{NDVI}_{\text{fine}}$ and $\text{NDVI}_{\text{coarse}}$ represents the aggregated NDVI value in a fine and coarse resolution. α is a linear regression coefficient, and ε is an error term. Lastly, s is an indicator for scene, implying that this relationship is tailored for each individual scene (221 scenes in this study).

However, the traditional TsHARP method is scene-specific, meaning that the linear relationship of NDVI and LST is established individually for each collocated time step. The reason for the scene-specific nature of the TsHARP method lies in the potential variation in the NDVI–LST relationship across different scenes, likely influenced by factors like the time of day. To meet our objective of creating LST data even outside these collocated time steps, we have generalized the approach. To address this, we generate the linear relationship for each hour of the day rather than for each individual scene, allowing for a more generalized application. This results in 24 individual TsHARP models representing each hour of the day. Mathematically, this can be expressed as Equation (4):

$$\text{LST}_{\text{fine}}(h) = \alpha(h) \times (\text{NDVI}_{\text{coarse}}(h) - \text{NDVI}_{\text{fine}}(h)) + \text{LST}_{\text{coarse}}(h) + \varepsilon(h) \tag{4}$$

In Equation (4), all variables remain consistent with Equation (3), except for h, an hour-of-the-day indicator. With the TsHARP method, we can calculate the downscaled LST at the 70 m-resolution as LST_{TsHARP}.

3.2. Extreme Gradient Boosting (XGB)

Extreme Gradient Boosting (XGBoost, hereafter XGB) is the primary machine-learning algorithm utilized in our study [64]. As part of the gradient boosting family, it operates by constructing multiple decision trees sequentially, where each subsequent tree corrects the errors of the previous ones. This iterative approach allows XGB to effectively learn from complex data patterns and improve prediction accuracy.

Here, we utilize nine predictor variables—LST_{2km}, $NDVI_{70m}$, $NDVI_{2km}$, $NDBI_{70m}$, $NDBI_{2km}$, $ELEV_{70m}$, $ELEV_{2km}$, hour of the day (HOD), and day of year (DOY)—to predict LST_{70m}. A notable advantage of our XGB is the handling of multicollinearity, particularly as NDVI and NDBI are often anti-correlated. Furthermore, by using information from both the 2 km- and 70 m-resolutions, rather than just their differences as in TsHARP, XGB can capture potential non-linearities in the influence of NDVI, NDBI, and ELEV on LST.

For the hyperparameter tuning on the XGB model, we employ a Bayesian optimization algorithm [65] to optimize the selection of hyperparameters, with an objective to minimize the root mean squared error (RMSE) of the model. This process involved 20 initial points, followed by 80 iterations, making a total of 100 estimation on the hyperparameter space. A list of hyperparameters with their descriptions and search ranges on the Bayesian optimization algorithm is shown in Table 1. Additionally, to avoid the risk of overfitting, we implement a five-fold cross-validation process. With the XGB method, we can calculate the downscaled LST at the 70 m-resolution as LST_{XGB}.

Table 1. Hyperparameter description and optimization details. The "Hyperparameter" and "Description" column show the name and description of hyperparameter utilized. The "Search Range" column indicates the range within which the Bayesian optimization algorithm sought optimal values. The "Selected Values" column shows the final hyperparameter values chosen by the optimizer.

Hyperparameter	Description	Search Range	Selected Value
max_depth	Maximum depth of a tree	[3, 10]	4
learning_rate	Boosting learning rate	[0.01, 0.3]	0.05
n_estimators	Number of gradient-boosted trees. Equivalent to number of boosting rounds	[50, 1200]	700
gamma	Minimum loss reduction required to make a further partition on a leaf node of the tree	[0, 5]	1
subsample	Subsample ratio of the training instance	[0.5, 1]	0.7
colsample_bytree	Subsample ratio of columns when constructing each tree	[0.5, 1]	0.75

3.3. Accuracy Verification with Evaluation Set

To assess the performance of the TsHARP and XGB, we divide the data into training and evaluation sets. We select four specific scenes from the available 221 collocated scenes, representing the hours of 0, 6, 12, and 18, as our evaluation sets, while all other scenes are selected as training sets. This selection is aimed at evaluating the models' ability to capture LST variations at different times and their diurnal cycles. Furthermore, these scenes are chosen based on having the second highest number of valid LST estimates in their respective hours, ensuring minimal cloud cover and maximum coverage by ECOSTRESS. Due to this selection threshold, the number of pixels in the training set is 92% of the total data, and the pixels in the evaluation set is 8% of the total data. The schematic of the model development, validation, and application are depicted in Figure 3.
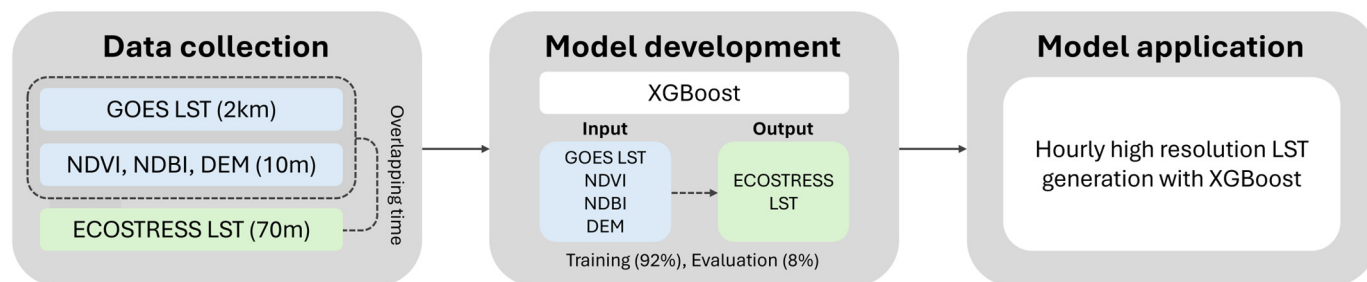
Figure 3. Schematic of data collection, model development, and application of XGBoost LST down-scaling model.

4. Downscaling Results

After training the TsHARP and XGB with the designated training sets (217 scenes, 92% of data) with a five-fold cross-validation process, we compare their performance against LST_{70m} from ECOSTRESS, in the evaluation sets (four scenes, 8% of data). The initial RMSE between ECOSTRESS and the nearest-neighbor-interpolated GOES data in the evaluation set was 3.14 °C. However, the RMSE improved to 2.46 °C for TsHARP and to 2.00 °C for XGB.

As a next step, we train TsHARP and XGB using all available collocated data for broader application. We maintained the same hyperparameters for the XGB as in the training phase to ensure there is no overfitting. Ultimately, the XGB model showed a superior performance compared to TsHARP, with a reduction in the RMSE by 0.61 °C and in the mean absolute error (MAE) by 0.40 °C, as depicted in Figure 4. The consistency of these results across both the evaluation set and the entire dataset suggests minimal overfitting in the XGB model and its enhanced effectiveness over TsHARP in predicting LST. Detailed statistics including r-squared value (RSQ) and MAE, as well as examples from the validation scenes, are presented in Figure 4.

Although XGBoost operates as a 'black box' model, preventing direct access to the equations of individual trees, we can still discern the significance of predictor variables through the model's feature importance function. Specifically, we employ the "Gain" function. This function quantifies the importance of each predictor by measuring the average gain of a feature when it is used in trees. By analyzing the gain values, we can determine which features contribute most to the model's decision-making process, offering insights into the underlying factors that drive the predictions, despite the inherent opacity of the XGBoost algorithm. Table 2 presents the feature importance of all predictor variables used in the development of the XGBoost algorithm. As observed in Table 2, HOD emerges as the most significant variable in our model, followed by NDBI, DOY, NDVI, and ELEV.

Table 2. Relative importance of predictor variables in the XGBoost model, calculated with the average gain of each feature when used in constructing the model's trees.

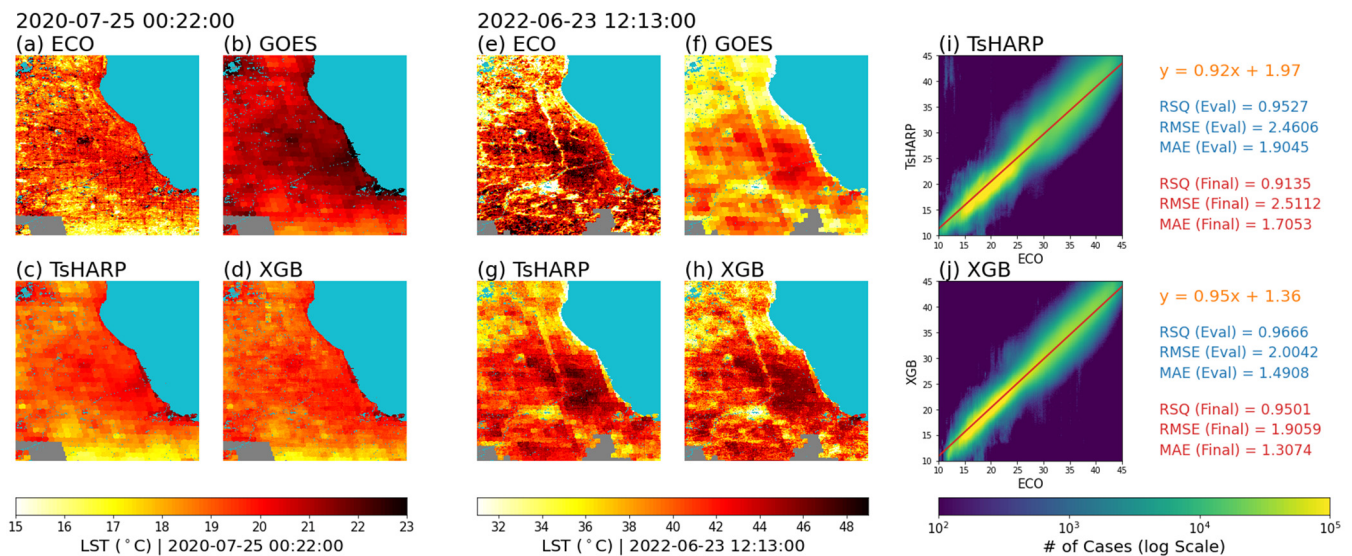| Variable	Abbreviation	Feature Importance
Hour of the day	HOD	0.1016
Day of year	DOY	0.0345
Normalized Difference Built-up Index	NDBI	0.0532
Normalized Difference Vegetation Index	NDVI	0.0142
Elevation	ELEV	0.0029

Figure 4. Comparative analysis of LST downscaling methods. (**a–d**) Downscaling result for 15 July 2020, at 00:22, with (**a**) LST data from ECOSTRESS (LST_{70m}), (**b**) GOES LST data (LST_{2km}), (**c**) TsHARP-downscaled LST (LST_{TsHARP}), and (**d**) XGB-downscaled LST (LST_{XGB}). Panels (**e–h**) show the same set for 23 June 2022, at 12:13. (**i**) Depiction of a heatmap comparing LST_{70m} with LST_{TsHARP} across the entire collocated dataset, including a linear fit equation in orange, and statistical metrics for the evaluation set in blue and for the final model in red. (**j**) Same as (**i**), but for LST_{70m} and LST_{XGB}. R squared, RMSE, and MAE values are also depicted in the figure for the Evaluation set (Eval, using 92% of data for training and tested on 8% of data) and the final model (Final, using all available data for training and testing).

5. Ethnic Inequality of LST Exposure in Chicago

5.1. City-Scale Ethnic Inequality

Employing the XGB downscaling technique enables us to refine GOES LST data to a higher resolution (70 m), irrespective of the availability of ECOSTRESS LST (application stage of the schematic in Figure 3). With GOES providing hourly LST estimates over Chicago, we can now obtain LST estimates at a 70 m resolution on an hourly basis. This enhanced spatiotemporal resolution of the LST data facilitates in-depth assessments at the neighborhood level. Utilizing this capability, we first apply our method to evaluate ethnic inequality in terms of the high LST in Chicago.

For our study, we selected target days from the GOES dataset over a five-year period based on specific criteria. Firstly, we focused on days during which more than 90% of the urban area of Chicago was under clear sky conditions for the entire 24 h period. This threshold was determined to be optimal after evaluating various levels, balancing data availability with the quantity of suitable observation days. Additionally, we focus on days with a minimum temperature exceeding 26 °C, representing the 75th percentile of the daily average LST in Chicago's urban regions. Applying these thresholds results in 10 days of nearly clear skies and high LST, we effectively identify what can be considered as some of the hottest days in Chicago. Following this, we apply the XGB downscaling, which provides us with hourly estimates of LST at a 70 m resolution for these selected 10 days.

We calculated the average LST_{XGB} for each block across all 240 h included in our selected 10-day period, capturing the 24 h diurnal LST_{XGB} cycle during Chicago's hottest days at the block level. We then computed the ethnicity-specific diurnal LST cycle for each block by applying a weighted average approach to LST_{XGB}, where the weights correspond to the percentage of each ethnic group within the block. Additionally, we conducted a same analysis using LST_{2km}, obtained through the nearest-neighbor interpolation of GOES LST data. This method allows us to compare the effects of downscaling on the diurnal LST cycles

specific to different ethnic groups. Chicago's ethnic distribution and its corresponding diurnal cycle of LST_{2km} and LST_{XGB} are depicted in Figure 5a–d.
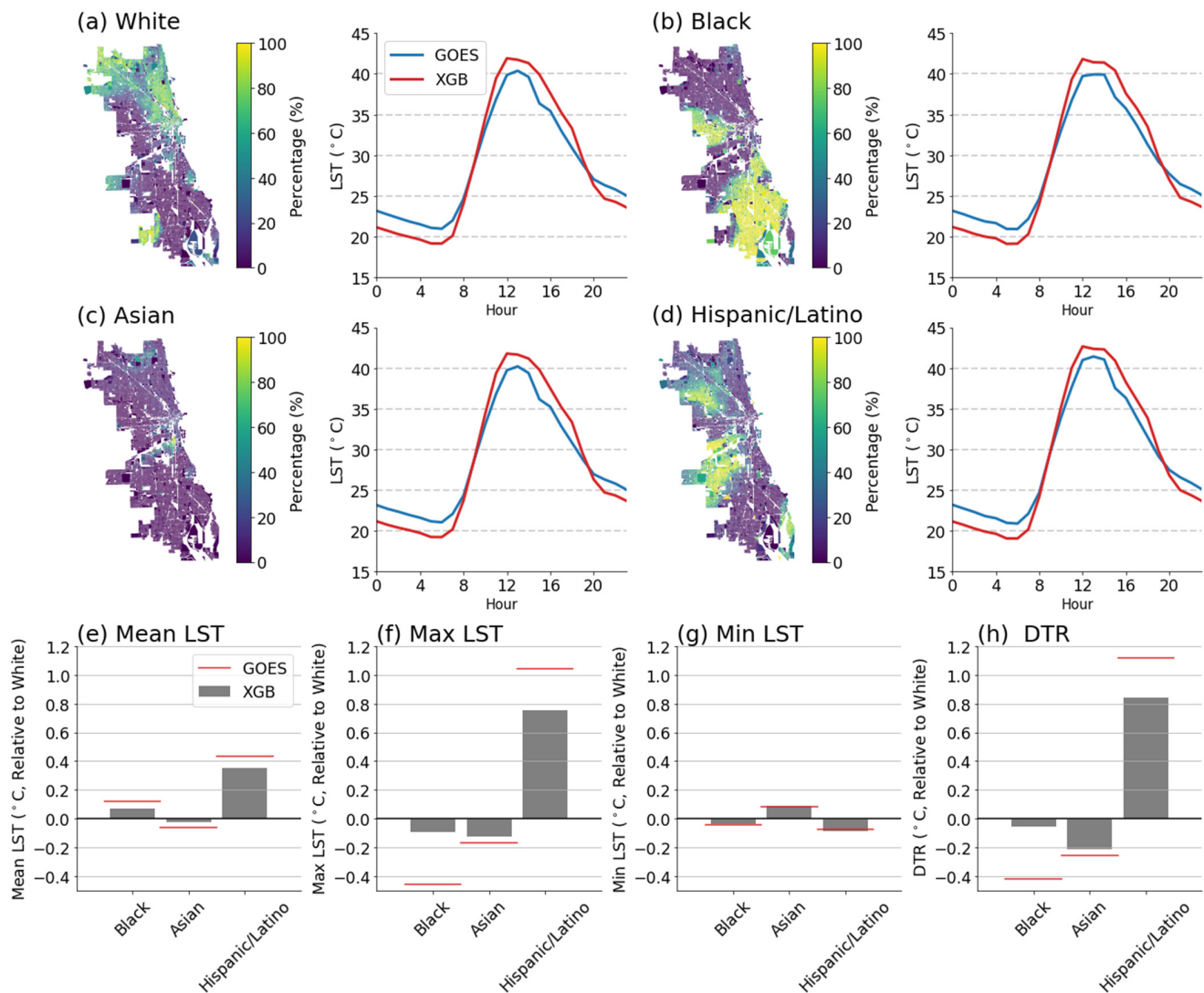

Figure 5. (**a**–**d**) Distribution of ethnicity (map) and corresponding diurnal cycle of LST obtained from LST_{2km} (blue) and LST_{XGB} (red) for (**a**) White, (**b**) Black, (**c**) Asian, and (**d**) Hispanic/Latino population. (**e**–**h**) Heat metric of each ethnicity, calculated as relative to White population. Metric calculated with LSTXGB are in gray bar, while values in LST_{2km} are in red line. (**e**) Mean, (**f**) maximum, (**g**) minimum LST, and (**h**) DTR of LST.

In Figure 5a–d, the diurnal LST cycle derived from the LST_{XGB} model demonstrates a more distinct variation compared to that from LST_{2km}. This higher variability is consistent across all ethnic demographics, showcasing the increased sensitivity of capturing the diurnal evolution of LST when using the downscaling method.

For a focused examination of ethnicity-specific heat exposure, we compute four LST metrics utilizing LST_{XGB} data: mean, maximum, minimum, and the diurnal temperature range (DTR). Figure 5e–h present bar graphs that illustrate the variance in these heat metrics among ethnic groups, with comparisons made relative to the White population. Both the mean and maximum LST (Figure 5e,f) indicate higher temperatures for the Hispanic/Latino populations compared to Whites. Conversely, the minimum LST differences are negligible among the ethnic groups, with a variation of less than 0.1 °C. The DTR depicted in Figure 5h reveals pronounced disparities, particularly for the Hispanic/Latino community, mostly

due to the high maximum LST during the day. Overall, we found that Hispanic/Latino communities are more exposed to higher LST and DTR.

However, while the LST_{XGB} captures greater diurnal variability in ethnic-specific LST compared to LST_{2km}, it does not highlight more significant ethnic differences in the mean, maximum, and DTR of LST. This is attributed to the fact that, although the XGB method detects a higher variation, the magnitude of these differences between ethnicities are less pronounced compared to those observed with LST_{2km}.

5.2. Regional Ethnicity Analysis on Humboldt Park

To delve deeper into ethnic inequalities with an emphasis on Hispanic/Latino communities, our analysis now focuses on the Humboldt Park region of Chicago. Humboldt Park has become a focal point for discussions in Chicago, regarding gentrification, which presents a complex tapestry of cultural shifts, economic development, and displacement pressures [66–68]. Furthermore, by concentrating our research on a more confined area of Humboldt Park, rather than the entire expanse of Chicago, we enhance our ability to discern the nuances and localized impacts of downscaling.

Figure 6a displays a demographic map of Humboldt Park, highlighting ethnic disparities at the block level. This is achieved by calculating the difference between Hispanic/Latino and White population percentages in each block. The resulting values, where larger numbers signify a higher prevalence of Hispanic/Latino over White populations, reveal a significant west–east gradient in the distribution of these ethnic groups. Moreover, areas with a Hispanic/Latino majority are characterized by distinct socio-economic patterns, as depicted in Figure 6b (economic hardship) and Figure 6c (educational attainment). Note that the analysis of these socio-economic metrics is conducted at the block group level, offering a coarser resolution compared to the ethnic data.

Figure 6b presents the hardship index, a measure of economic adversity where higher scores denote greater hardship. Figure 6c illustrates the educational metric, which quantifies the proportion of the population with a high school diploma. The data illustrated in these figures indicate that, within Humboldt Park, communities predominantly comprising Hispanic/Latino individuals tend to face greater economic disadvantages and exhibit lower educational attainment levels. Both exhibit strong correlations with the Hispanic/Latino population percentage, with R² values of 0.56 and 0.49, respectively, underscoring a profound association between ethnic composition and socio-economic factors in the region.

We match these data with the maximum LST_{XGB} during the 10 hottest days in Chicago, as calculated from the previous section (Figure 6d). In the Humboldt Park region, there is a strong, positive relationship between the block-level Hispanic/Latino population ratio and maximum LST (Figure 6e). Block-groups with predominantly Hispanic/Latino populations tend to experience greater maximum temperatures than blocks with predominantly White populations. Calculating the linear fit ($R^2 = 0.52$) between the ethnic difference and maximum LST, we find that blocks completely constituted with Hispanic/Latino residents show a maximum LST that is 1.5 °C higher compared to blocks with solely White residents.

We calculate the same statistics using LST_{2km}. The results, evident in Figure 6f,g, demonstrate that employing LST_{2km} notably reduces the spatial variability of LST. When calculating the linear relationship between ethnic differences and LST_{2km}, both the slope and the R^2 value decrease. This suggests that, while using a downscaled LST may not significantly impact the assessment of ethnic differences at the city level (as shown in Figure 5), it plays a crucial role in analyzing ethnic inequality at a regional level, such as in Humboldt Park.
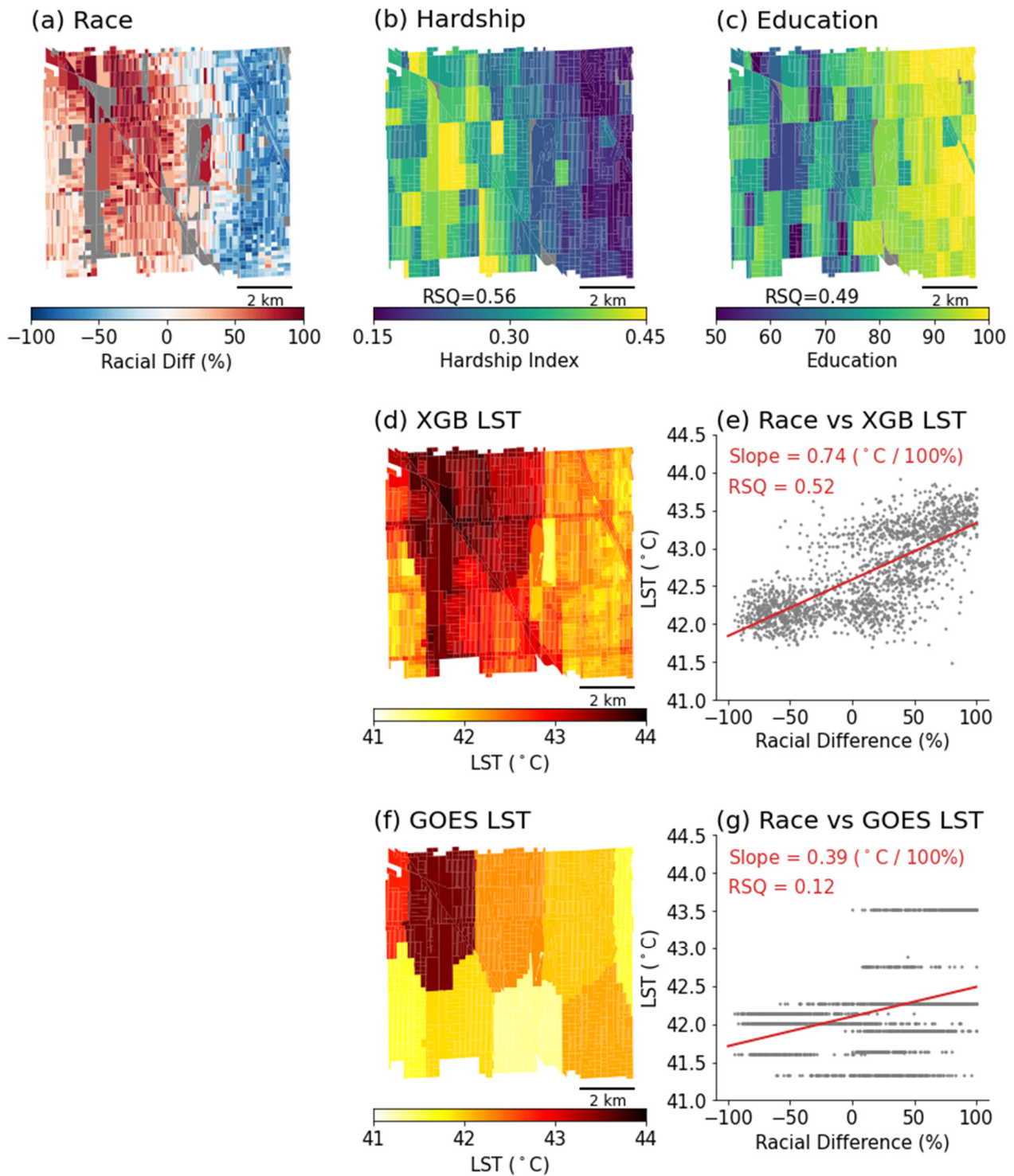
Figure 6. (**a**) Ethnic map of Humboldt Park region, where ethnic difference is calculated as Hispanic/Latino percentage minus White percentage. Red colors show blocks predominantly inhabited by Hispanic/Latino residents, while blue shows the blocks that are home to White residents. (**b**) Map of economic hardship index for Humboldt Park region. (**c**) Map of educational attainment in Humboldt Park region. (**d**) Maximum LST_{XGB} map for Humboldt Park region, calculated from 10 clear-sky hottest day in Chicago. (**e**) Scatterplot and linear fit of relationship between ethnic difference and maximum LST_{XGB}. (**f,g**) Same as (**d,e**), but with LST_{2km}.

6. Discussions and Conclusions

In this study, we developed an XGBoost-based algorithm to downscale 2 km-resolution LST data from the GOES satellite to a finer 70 m resolution, utilizing ancillary variables including NDVI, NDBI, and DEM. This method outperformed the conventional TsHARP technique, achieving a lower RMSE of 1.90 °C compared to 2.51 °C for TsHARP. The distinctive aspect of our approach is its reliance on data from the geostationary satellite GOES and the high-resolution estimate from ECOSTRESS with an irregular revisit period, facilitating hourly LST downscaling, which is vital for acquiring high-resolution LST data consistently throughout the day. Prior research predominantly focused on LST measurements taken once daily [8,45,69], an approach that may not adequately capture the complete diurnal cycle of LST. Additionally, our methodology has the potential for broader application across North America, leveraging the global observational reach of ECOSTRESS and the North America-focused capabilities of GOES.

To demonstrate the utility of these data, we assessed a 70 m-resolution LST on Chicago's hottest days and investigated its association with ethnic inequality. Our findings reveal that the Hispanic/Latino communities endure the highest LST and variability, evidenced by an elevated maximum LST and DTR. Although LST is not a direct indicator of human exposure to high temperatures, its relevance as a proxy is supported by the previous research on thermal comfort [70–72]. Given the previous research indicating the limited healthcare access for Hispanic/Latino communities in Chicago [73], the observed temperature extremes could disproportionately amplify the risk of temperature-related health issues within these populations [74,75]. Furthermore, in Chicago, gentrification frequently impacts Hispanic/Latino communities [76–78], a process associated with reduced access to green spaces [79] that can increase LST [80–82] and exacerbate health outcomes [83].

To deepen our understanding of the impact of gentrification, we focus on Chicago's Humboldt Park, an area notably affected by such changes. Within this region, we observed that blocks predominantly inhabited by Hispanic/Latino residents, who are economically and educationally disadvantaged, display a maximum LST that is 1.5 °C higher than blocks predominantly occupied by White residents. This disparity highlights the intersection of urban development and ethnic inequality, revealing how gentrification can lead to environmental inequities. The use of downscaled LST data, derived from our developed XGBoost downscaling method, enhances the spatial resolution of our analysis, allowing for a more precise and localized examination of these temperature disparities. Additionally, unlike data from ECOSTRESS, which is limited by its return period, our downscaled method enables the estimation of high-resolution LST on an hourly basis, providing a more continuous temporal resolution. This capability allows for a more detailed understanding of how LST varies throughout the day, offering insights into the diurnal patterns that affect urban heat distribution and the resulting impacts on the community's residents. This refined approach offers a clearer, more granular understanding of how urban changes affect different segments of the population, highlighting the critical need for targeted urban planning and interventions.

Overall, our findings indicate that, in Chicago, the populations with the fewest resources to combat high temperatures are those most exposed to elevated LST. This discovery is pivotal for policymakers, as it underscores the urgency of targeted urban planning interventions, such as augmenting green spaces within underrepresented communities. The significance of such measures is compounded by the existing inequality in the distribution of green spaces across Chicago [48], further emphasizing the need for equitable access to these critical urban infrastructures.

While this study provides significant insights, there is uncertainty involved and room for improvement. Firstly, the accuracy of LST estimates from both GOES and ECOSTRESS can cause uncertainty [52,55,84–87] as factors such as different observation angles can influence the LST measurements [88]. Since the purpose of this study is to downscale the 2 km satellite-based LST to 70 m satellite-based LST estimates, inherent uncertainties in satellite LST measurements are unavoidable. To address this, in situ measurements of LST

from meteorological stations of flux towers could be utilized. However, incorporating these measurements is outside the scope of the current study, although it represents a promising direction for future research. Secondly, incorporating metrics beyond LST, such as a 2 m air temperature and humidity, could enhance the direct analysis of health outcomes and community impacts. These metrics, which cannot be directly estimated from satellite data, would need additional research and methodological advancements, such as incorporating ground-based lidar or a temperature measuring campaign [89]. Lastly, LST measurements are perforumed under clear sky conditions. Other downscaling methods rather than using satellite estimates can overcome this limitation [90–92].

Conflicts of Interest: The authors declare no conflicts of interest.

References

1. Yang, J.; Yang, Y.; Sun, D.; Jin, C.; Xiao, X. Influence of urban morphological characteristics on thermal environment. *Sustain. Cities Soc.* **2021**, *72*, 103045. [CrossRef]
2. Chen, F.; Yang, S.; Yin, K.; Chan, P. Challenges to quantitative applications of Landsat observations for the urban thermal environment. *J. Environ. Sci.* **2017**, *59*, 80–88. [CrossRef] [PubMed]
3. Sharifi, A.; Pathak, M.; Joshi, C.; He, B.-J. A systematic review of the health co-benefits of urban climate change adaptation. *Sustain. Cities Soc.* **2021**, *74*, 103190. [CrossRef]
4. Moonen, P.; Defraeye, T.; Dorer, V.; Blocken, B.; Carmeliet, J. Urban Physics: Effect of the micro-climate on comfort, health and energy demand. *Front. Archit. Res.* **2012**, *1*, 197–228. [CrossRef]
5. Mashhoodi, B. Environmental justice and surface temperature: Income, ethnic, gender, and age inequalities. *Sustain. Cities Soc.* **2021**, *68*, 102810. [CrossRef]
6. Renteria, R.; Grineski, S.; Collins, T.; Flores, A.; Trego, S. Social disparities in neighborhood heat in the Northeast United States. *Environ. Res.* **2022**, *203*, 111805. [CrossRef]
7. Mitchell, B.C.; Chakraborty, J. Exploring the relationship between residential segregation and thermal inequity in 20 US cities. *Local Environ.* **2018**, *23*, 796–813. [CrossRef]
8. Dialesandro, J.; Brazil, N.; Wheeler, S.; Abunnasr, Y. Dimensions of thermal inequity: Neighborhood social demographics and urban heat in the Southwestern US. *Int. J. Environ. Res. Public Health* **2021**, *18*, 941. [CrossRef] [PubMed]
9. Feng, X.; Myint, S.W. Exploring the effect of neighboring land cover pattern on land surface temperature of central building objects. *Build. Environ.* **2016**, *95*, 346–354. [CrossRef]
10. Alexander, C. Normalised difference spectral indices and urban land cover as indicators of land surface temperature (LST). *Int. J. Appl. Earth Obs. Geoinf.* **2020**, *86*, 102013. [CrossRef]
11. Tetali, S.; Baird, N.; Klima, K. A multicity analysis of daytime Surface Urban Heat Islands in India and the US. *Sustain. Cities Soc.* **2022**, *77*, 103568. [CrossRef]

12. Guha, S.; Govil, H.; Dey, A.; Gill, N. Analytical study of land surface temperature with NDVI and NDBI using Landsat 8 OLI and TIRS data in Florence and Naples city, Italy. *Eur. J. Remote Sens.* **2018**, *51*, 667–678. [CrossRef]

13. Gage, E.A.; Cooper, D.J. Urban forest structure and land cover composition effects on land surface temperature in a semi-arid suburban area. *Urban For. Urban Green.* **2017**, *28*, 28–35. [CrossRef]

14. Fu, P.; Weng, Q. Variability in annual temperature cycle in the urban areas of the United States as revealed by MODIS imagery. *ISPRS J. Photogramm. Remote Sens.* **2018**, *146*, 65–73. [CrossRef]

15. Al-Hamdan, M.Z.; Quattrochi, D.A.; Bounoua, L.; Lachir, A.; Zhang, P. Using Landsat, MODIS, and a biophysical model to evaluate LST in urban centers. *Remote Sens.* **2016**, *8*, 952. [CrossRef]

16. Mukherjee, S.; Joshi, P.; Garg, R.D. Analysis of urban built-up areas and surface urban heat island using downscaled MODIS derived land surface temperature data. *Geocarto Int.* **2017**, *32*, 900–918. [CrossRef]

17. Keramitsoglou, I.; Kiranoudis, C.T.; Ceriola, G.; Weng, Q.; Rajasekar, U. Identification and analysis of urban surface temperature patterns in Greater Athens, Greece, using MODIS imagery. *Remote Sens. Environ.* **2011**, *115*, 3080–3090. [CrossRef]

18. Elmes, A.; Healy, M.; Geron, N.; Andrews, M.; Rogan, J.; Martin, D.; Sangermano, F.; Williams, C.; Weil, B. Mapping spatiotemporal variability of the urban heat island across an urban gradient in Worcester, Massachusetts using in-situ Thermochrons and Landsat-8 Thermal Infrared Sensor (TIRS) data. *GISci. Remote Sens.* **2020**, *57*, 845–864. [CrossRef]

19. Hulley, G.; Shivers, S.; Wetherley, E.; Cudd, R. New ECOSTRESS and MODIS land surface temperature data reveal fine-scale heat vulnerability in cities: A case study for Los Angeles County, California. *Remote Sens.* **2019**, *11*, 2136. [CrossRef]

20. Chang, Y.; Xiao, J.; Li, X.; Middel, A.; Zhang, Y.; Gu, Z.; Wu, Y.; He, S. Exploring diurnal thermal variations in urban local climate zones with ECOSTRESS land surface temperature data. *Remote Sens. Environ.* **2021**, *263*, 112544. [CrossRef]

21. Liu, Y.; Xu, X.; Wang, F.; Qiao, Z.; An, H.; Han, D.; Luo, J. Exploring the cooling effect of urban parks based on the ECOSTRESS land surface temperature. *Front. Ecol. Evol.* **2022**, *10*, 1031517. [CrossRef]

22. Yao, X.; Zeng, X.; Zhu, Z.; Lan, Y.; Shen, Y.; Liu, Q.; Yang, F. Exploring the diurnal variations of the driving factors affecting block-based LST in a "Furnace city" using ECOSTRESS thermal imaging. *Sustain. Cities Soc.* **2023**, *98*, 104841. [CrossRef]

23. Chang, Y.; Xiao, J.; Li, X.; Zhou, D.; Wu, Y. Combining GOES-R and ECOSTRESS land surface temperature data to investigate diurnal variations of surface urban heat island. *Sci. Total Environ.* **2022**, *823*, 153652. [CrossRef] [PubMed]

24. Chang, Y.; Xiao, J.; Li, X.; Weng, Q. Monitoring diurnal dynamics of surface urban heat island for urban agglomerations using ECOSTRESS land surface temperature observations. *Sustain. Cities Soc.* **2023**, *98*, 104833. [CrossRef]

25. Han, D.; An, H.; Cai, H.; Wang, F.; Xu, X.; Qiao, Z.; Jia, K.; Sun, Z.; An, Y. How do 2D/3D urban landscapes impact diurnal land surface temperature: Insights from block scale and machine learning algorithms. *Sustain. Cities Soc.* **2023**, *99*, 104933. [CrossRef]

26. Lin, Z.; Xu, H.; Yao, X.; Yang, C.; Ye, D. How does urban thermal environmental factors impact diurnal cycle of land surface temperature? A multi-dimensional and multi-granularity perspective. *Sustain. Cities Soc.* **2024**, *101*, 105190. [CrossRef]

27. Chang, Y.; Xiao, J.; Li, X.; Frolking, S.; Zhou, D.; Schneider, A.; Weng, Q.; Yu, P.; Wang, X.; Li, X. Exploring diurnal cycles of surface urban heat island intensity in Boston with land surface temperature data derived from GOES-R geostationary satellites. *Sci. Total Environ.* **2021**, *763*, 144224. [CrossRef] [PubMed]

28. Hrisko, J.; Ramamurthy, P.; Yu, Y.; Yu, P.; Melecio-Vázquez, D. Urban air temperature model using GOES-16 LST and a diurnal regressive neural network algorithm. *Remote Sens. Environ.* **2020**, *237*, 111495. [CrossRef]

29. Hrisko, J.; Ramamurthy, P.; Melecio-Vázquez, D.; Gonzalez, J.E. Spatiotemporal Variability of Heat Storage in Major US Cities—A Satellite-Based Analysis. *Remote Sens.* **2020**, *13*, 59. [CrossRef]

30. Beale, C.; Norouzi, H.; Sharifnezhadazizi, Z.; Bah, A.R.; Yu, P.; Yu, Y.; Blake, R.; Vaculik, A.; Gonzalez-Cruz, J. Comparison of diurnal variation of land surface temperature from GOES-16 ABI and MODIS instruments. *IEEE Geosci. Remote Sens. Lett.* **2019**, *17*, 572–576. [CrossRef]

31. Ha, W.; Gowda, P.H.; Howell, T.A. Downscaling of land surface temperature maps in the Texas high plains with the TsHARP method. *GISci. Remote Sens.* **2011**, *48*, 583–599. [CrossRef]

32. Agam, N.; Kustas, W.P.; Anderson, M.C.; Li, F.; Colaizzi, P.D. Utility of thermal sharpening over Texas high plains irrigated agricultural fields. *J. Geophys. Res. Atmos.* **2007**, *112*, D19110. [CrossRef]

33. Chen, X.; Li, W.; Chen, J.; Rao, Y.; Yamaguchi, Y. A combination of TsHARP and thin plate spline interpolation for spatial sharpening of thermal imagery. *Remote Sens.* **2014**, *6*, 2845–2863. [CrossRef]

34. Inamdar, A.K.; French, A. Disaggregation of GOES land surface temperatures using surface emissivity. *Geophys. Res. Lett.* **2009**, *36*, L02408. [CrossRef]

35. Hais, M.; Kučera, T. The influence of topography on the forest surface temperature retrieved from Landsat TM, ETM+ and ASTER thermal channels. *ISPRS J. Photogramm. Remote Sens.* **2009**, *64*, 585–591. [CrossRef]

36. Maeda, E.E. Downscaling MODIS LST in the East African mountains using elevation gradient and land-cover information. *Int. J. Remote Sens.* **2014**, *35*, 3094–3108. [CrossRef]

37. Zhang, X.; Zhao, H.; Yang, J. Spatial downscaling of land surface temperature in combination with TVDI and elevation. *Int. J. Remote Sens.* **2019**, *40*, 1875–1886. [CrossRef]

38. Hutengs, C.; Vohland, M. Downscaling land surface temperatures at regional scales with random forest regression. *Remote Sens. Environ.* **2016**, *178*, 127–141. [CrossRef]

39. Pu, R. Assessing scaling effect in downscaling land surface temperature in a heterogenous urban environment. *Int. J. Appl. Earth Obs. Geoinf.* **2021**, *96*, 102256. [CrossRef]

40. Li, W.; Ni, L.; Li, Z.-l.; Duan, S.-B.; Wu, H. Evaluation of machine learning algorithms in spatial downscaling of MODIS land surface temperature. *IEEE J. Sel. Top. Appl. Earth Obs. Remote Sens.* **2019**, *12*, 2299–2307. [CrossRef]

41. Tu, H.; Cai, H.; Yin, J.; Zhang, X.; Zhang, X. Land surface temperature downscaling in the karst mountain urban area considering the topographic characteristics. *J. Appl. Remote Sens.* **2022**, *16*, 034515. [CrossRef]

42. Anderson, B.G.; Bell, M.L. Weather-related mortality: How heat, cold, and heat waves affect mortality in the United States. *Epidemiology* **2009**, *20*, 205. [CrossRef] [PubMed]

43. Mashhoodi, B. Feminization of surface temperature: Environmental justice and gender inequality among socioeconomic groups. *Urban Clim.* **2021**, *40*, 101004. [CrossRef]

44. Zhu, Y.; Myint, S.W.; Schaffer-Smith, D.; Muenich, R.L.; Tong, D.; Li, Y. Formulating operational mitigation options and examining intra-urban social inequality using evidence-based urban warming effects. *Front. Environ. Sci.* **2022**, *9*, 795474. [CrossRef]

45. Mitchell, B.C.; Chakraborty, J. Landscapes of thermal inequity: Disproportionate exposure to urban heat in the three largest US cities. *Environ. Res. Lett.* **2015**, *10*, 115005. [CrossRef]

46. Benz, S.A.; Burney, J.A. Widespread race and class disparities in surface urban heat extremes across the United States. *Earth's Future* **2021**, *9*, e2021EF002016. [CrossRef]

47. Hsu, A.; Sheriff, G.; Chakraborty, T.; Manya, D. Disproportionate exposure to urban heat island intensity across major US cities. *Nat. Commun.* **2021**, *12*, 2721. [CrossRef]

48. Liu, D.; Kwan, M.-P.; Kan, Z. Analysis of urban green space accessibility and distribution inequity in the City of Chicago. *Urban For. Urban Green.* **2021**, *59*, 127029. [CrossRef]

49. Williams, T.G.; Logan, T.M.; Zuo, C.T.; Liberman, K.D.; Guikema, S.D. Parks and safety: A comparative study of green space access and inequity in five US cities. *Landsc. Urban Plan.* **2020**, *201*, 103841. [CrossRef]

50. Schmit, T.J.; Gunshor, M.M.; Menzel, W.P.; Gurka, J.J.; Li, J.; Bachmeier, A.S. Introducing the next-generation Advanced Baseline Imager on GOES-R. *Bull. Am. Meteorol. Soc.* **2005**, *86*, 1079–1096. [CrossRef]

51. Ching, J.; Mills, G.; Bechtel, B.; See, L.; Feddema, J.; Wang, X.; Ren, C.; Brousse, O.; Martilli, A.; Neophytou, M. WUDAPT: An urban weather, climate, and environmental modeling infrastructure for the anthropocene. *Bull. Am. Meteorol. Soc.* **2018**, *99*, 1907–1924. [CrossRef]

52. Yu, Y.; Tarpley, D.; Privette, J.L.; Flynn, L.E.; Xu, H.; Chen, M.; Vinnikov, K.Y.; Sun, D.; Tian, Y. Validation of GOES-R satellite land surface temperature algorithm using SURFRAD ground measurements and statistical estimates of error properties. *IEEE Trans. Geosci. Remote Sens.* **2011**, *50*, 704–713. [CrossRef]

53. Yu, Y.; Yu, P. Land surface temperature product from the GOES-R series. In *The GOES-R Series*; Elsevier: Amsterdam, The Netherlands, 2020; pp. 133–144.

54. Hulley, G.C.; Göttsche, F.M.; Rivera, G.; Hook, S.J.; Freepartner, R.J.; Martin, M.A.; Cawse-Nicholson, K.; Johnson, W.R. Validation and quality assessment of the ECOSTRESS level-2 land surface temperature and emissivity product. *IEEE Trans. Geosci. Remote Sens.* **2021**, *60*, 5000523. [CrossRef]

55. Guha, S.; Govil, H.; Gill, N.; Dey, A. A long-term seasonal analysis on the relationship between LST and NDBI using Landsat data. *Quat. Int.* **2021**, *575*, 249–258. [CrossRef]

56. Guo, A.; Yang, J.; Sun, W.; Xiao, X.; Cecilia, J.X.; Jin, C.; Li, X. Impact of urban morphology and landscape characteristics on spatiotemporal heterogeneity of land surface temperature. *Sustain. Cities Soc.* **2020**, *63*, 102443. [CrossRef]

57. Guha, S.; Govil, H. Seasonal variability of LST-NDVI correlation on different land use/land cover using Landsat satellite sensor: A case study of Raipur City, India. *Environ. Dev. Sustain.* **2022**, *24*, 8823–8839. [CrossRef]

58. Gascon, F.; Bouzinac, C.; Thépaut, O.; Jung, M.; Francesconi, B.; Louis, J.; Lonjou, V.; Lafrance, B.; Massera, S.; Gaudel-Vacaresse, A. Copernicus Sentinel-2A calibration and products validation status. *Remote Sens.* **2017**, *9*, 584. [CrossRef]

59. Maune, D.F.; Kopp, S.; Zerdas, C. Digital elevation model technologies and applications. In *The DEM Users Manual*; American Society for Photogrammetry and Remote Sensing: Bethesda, MD, USA, 2007.

60. Gesch, D.B.; Oimoen, M.J.; Evans, G.A. *Accuracy Assessment of the US Geological Survey National Elevation Dataset, and Comparison with other Large-Area Elevation Datasets: SRTM and ASTER*; US Department of the Interior, US Geological Survey: Sioux Falls, SD, USA, 2014; Volume 1008.

61. Sattari, F.; Hashim, M.; Sookhak, M.; Banihashemi, S.; Pour, A.B. Assessment of the TsHARP method for spatial downscaling of land surface temperature over urban regions. *Urban Clim.* **2022**, *45*, 101265. [CrossRef]

62. Mukherjee, S.; Joshi, P.; Garg, R.D. A comparison of different regression models for downscaling Landsat and MODIS land surface temperature images over heterogeneous landscape. *Adv. Space Res.* **2014**, *54*, 655–669. [CrossRef]

63. Sattari, F.; Hashim, M.; Pour, A.B. Thermal sharpening of land surface temperature maps based on the impervious surface index with the TsHARP method to ASTER satellite data: A case study from the metropolitan Kuala Lumpur, Malaysia. *Measurement* **2018**, *125*, 262–278. [CrossRef]

64. Chen, T.; Guestrin, C. Xgboost: A scalable tree boosting system. In Proceedings of the 22nd ACM Sigkdd International Conference on Knowledge Discovery and Data Mining, San Francisco, CA, USA, 13–17 August 2016; pp. 785–794.

65. Snoek, J.; Larochelle, H.; Adams, R.P. Practical bayesian optimization of machine learning algorithms. *Adv. Neural Inf. Process. Syst.* **2012**, *25*, 2951.

66. Mumm, J. Gentrification in color and time: White and Puerto Rican racial histories at work in Humboldt Park. *Cent. J.* **2016**, *28*, 88–125.

67. Wilson, D.; Grammenos, D. Gentrification, discourse, and the body: Chicago's Humboldt Park. *Environ. Plan. D Soc. Space* **2005**, *23*, 295–312. [CrossRef]

68. Rinaldo, R. Space of resistance: The Puerto Rican cultural center and Humboldt Park. *Cult. Crit.* **2002**, *50*, 135–174. [CrossRef]

69. Chakraborty, T.; Hsu, A.; Manya, D.; Sheriff, G. Disproportionately higher exposure to urban heat in lower-income neighborhoods: A multi-city perspective. *Environ. Res. Lett.* **2019**, *14*, 105003. [CrossRef]

70. Goldblatt, R.; Addas, A.; Crull, D.; Maghrabi, A.; Levin, G.G.; Rubinyi, S. Remotely sensed derived land surface temperature (LST) as a proxy for air temperature and thermal comfort at a small geographical scale. *Land* **2021**, *10*, 410. [CrossRef]

71. Patel, S.; Indraganti, M.; Jawarneh, R.N. A comprehensive systematic review: Impact of Land Use/Land Cover (LULC) on Land Surface Temperatures (LST) and outdoor thermal comfort. *Build. Environ.* **2023**, *249*, 111130. [CrossRef]

72. Imran, H.; Hossain, A.; Islam, A.S.; Rahman, A.; Bhuiyan, M.A.E.; Paul, S.; Alam, A. Impact of land cover changes on land surface temperature and human thermal comfort in Dhaka city of Bangladesh. *Earth Syst. Environ.* **2021**, *5*, 667–693. [CrossRef]

73. Lee, H.; Caldwell, J.T.; Maene, C.; Cagney, K.A.; Saunders, M.R. Racial/ethnic inequities in access to high-quality dialysis treatment in Chicago: Does neighborhood racial/ethnic composition matter? *J. Racial Ethn. Health Disparities* **2020**, *7*, 854–864. [CrossRef]

74. Lee, J.; Dessler, A.E. Future Temperature-Related Deaths in the US: The Impact of Climate Change, Demographics, and Adaptation. *GeoHealth* **2023**, *7*, e2023GH000799. [CrossRef]

75. Davis, R.E.; Hondula, D.M.; Sharif, H. Examining the diurnal temperature range enigma: Why is human health related to the daily change in temperature? *Int. J. Biometeorol.* **2020**, *64*, 397–407. [CrossRef] [PubMed]

76. Betancur, J.J. The politics of gentrification: The case of West Town in Chicago. *Urban Aff. Rev.* **2002**, *37*, 780–814. [CrossRef]

77. Mumm, J. The racial fix: White currency in the gentrification of black and Latino Chicago. *Focaal* **2017**, *2017*, 102–118. [CrossRef]

78. Orta, D. "Mexicans Built This Neighborhood!" Gentrification, Organizations, and the Role of Place-Based Identity in Latinx Chicago. *Soc. Sci.* **2021**, *10*, 304. [CrossRef]

79. Francis, J.; Disney, M.; Law, S. Monitoring canopy quality and improving equitable outcomes of urban tree planting using LiDAR and machine learning. *Urban For. Urban Green.* **2023**, *89*, 128115. [CrossRef]

80. Schwaab, J.; Meier, R.; Mussetti, G.; Seneviratne, S.; Bürgi, C.; Davin, E.L. The role of urban trees in reducing land surface temperatures in European cities. *Nat. Commun.* **2021**, *12*, 6763. [CrossRef] [PubMed]

81. Wang, J.; Zhou, W.; Jiao, M. Location matters: Planting urban trees in the right places improves cooling. *Front. Ecol. Environ.* **2022**, *20*, 147–151. [CrossRef]

82. Zhou, W.; Wang, J.; Cadenasso, M.L. Effects of the spatial configuration of trees on urban heat mitigation: A comparative study. *Remote Sens. Environ.* **2017**, *195*, 1–12. [CrossRef]

83. Cole, H.V.; Triguero-Mas, M.; Connolly, J.J.; Anguelovski, I. Determining the health benefits of green space: Does gentrification matter? *Health Place* **2019**, *57*, 1–11. [CrossRef]

84. Li, K.; Guan, K.; Jiang, C.; Wang, S.; Peng, B.; Cai, Y. Evaluation of four new land surface temperature (LST) products in the US corn belt: ECOSTRESS, GOES-R, landsat, and sentinel-3. *IEEE J. Sel. Top. Appl. Earth Obs. Remote Sens.* **2021**, *14*, 9931–9945. [CrossRef]

85. Sun, D.; Yu, Y.; Fang, L.; Liu, Y. Toward an operational land surface temperature algorithm for GOES. *J. Appl. Meteorol. Climatol.* **2013**, *52*, 1974–1986. [CrossRef]

86. Xu, H.; Yu, Y.; Tarpley, D.; Göttsche, F.-M.; Olesen, F.-S. Evaluation of GOES-R land surface temperature algorithm using SEVIRI satellite retrievals with in situ measurements. *IEEE Trans. Geosci. Remote Sens.* **2013**, *52*, 3812–3822. [CrossRef]

87. Meng, X.; Cheng, J.; Yao, B.; Guo, Y. Validation of the ECOSTRESS land surface temperature product using ground measurements. *IEEE Geosci. Remote Sens. Lett.* **2021**, *19*, 3005305. [CrossRef]

88. Bian, Z.; Roujean, J.-L.; Lagouarde, J.-P.; Cao, B.; Li, H.; Du, Y.; Liu, Q.; Xiao, Q.; Liu, Q. A semi-empirical approach for modeling the vegetation thermal infrared directional anisotropy of canopies based on using vegetation indices. *ISPRS J. Photogramm. Remote Sens.* **2020**, *160*, 136–148. [CrossRef]

89. Kraemer, R.; Remmler, P.; Bumberger, J.; Kabisch, N. Running a dense air temperature measurement field campaign at the urban neighbourhood level: Protocol and lessons learned. *MethodsX* **2022**, *9*, 101719. [CrossRef] [PubMed]

90. Zhang, X.; Zhou, J.; Liang, S.; Wang, D. A practical reanalysis data and thermal infrared remote sensing data merging (RTM) method for reconstruction of a 1-km all-weather land surface temperature. *Remote Sens. Environ.* **2021**, *260*, 112437. [CrossRef]

91. Long, D.; Yan, L.; Bai, L.; Zhang, C.; Li, X.; Lei, H.; Yang, H.; Tian, F.; Zeng, C.; Meng, X. Generation of MODIS-like land surface temperatures under all-weather conditions based on a data fusion approach. *Remote Sens. Environ.* **2020**, *246*, 111863. [CrossRef]

92. Duan, S.-B.; Lian, Y.; Zhao, E.; Chen, H.; Han, W.; Wu, Z. A Novel Approach to All-Weather LST Estimation using XGBoost Model and Multi-Source Data. *IEEE Trans. Geosci. Remote Sens.* **2023**, *61*, 5004614. [CrossRef]